




Large-scale Dynamics of Line-driven Winds with the Re-radiation Effect

Yi Zhu¹  and Jinsen Xie

School of Nuclear Science and Technology, University of South China, Hengyang 421001, China; jinsen_xie@usc.edu.cn

Received 2023 April 13; revised 2023 June 21; accepted 2023 July 20; published 2023 October 31

Abstract

Previous simulations studying winds only focus on the line force due to photons from central active galactic nuclei. What properties of the winds will be when including the re-radiation force due to the scattered and reprocessed photons (i.e., the re-radiation effect)? We perform simulations to study the large-scale dynamics of accretion disk winds driven by radiation line force and re-radiation force. For the fiducial run, we find that the re-radiation force drives stronger outflows during the early stages. When the flows get into the steadiness, the UV radiation due to spectral lines dominates total radiation and the re-radiation effect could be negligible. The opening angle of winds narrows as the initial gas density increases. The larger the gas density is, the stronger the re-radiation effect will be. For $M_{\text{BH}} = 10^6 M_{\odot}$, $\varepsilon = 0.3$, the outflows do become much stronger with the re-radiation effect and the winds still cannot escape from gravitational potential. We find that the detection probability of ultra-fast outflows and the properties of the winds are both consistent with the observations.

Key words: accretion – accretion disks – black hole physics – galaxies: nuclei – stars: winds – outflows

1. Introduction

Observations evidences of low luminosity active galactic nuclei (AGNs) (Crenshaw et al. 2003; Tombesi et al. 2010, 2014) and black hole X-ray binaries (Neilsen & Homan 2012; Homan et al. 2016) show that winds are common phenomenon. It is believed that winds play a momentous role in AGNs feedback. Both winds and AGNs radiation can interact with their host galaxies (Zhang et al. 2021; Lin et al. 2022). The radiation from AGNs can heat the interstellar medium (ISM) and affect the properties of ISM (Ciotti et al. 2009; Yuan & Narayan 2014). The winds can interact with ISM effectively and result in their co-evolution (Ostriker et al. 2010; Weinberger et al. 2017; Yuan et al. 2018; Lin et al. 2022).

Accretion flows of a black hole can be divided into hot accretion flows and cold accretion flows. Hot accretion flows are highly hot and optically thin, and found at lower mass accretion rates systems. Winds from hot accretion flows have been directly detected in the low-luminosity AGNs (Almeida et al. 2018; Ma et al. 2019; Shi et al. 2021) and black hole X-ray binaries (Homan et al. 2016; Munoz-Darias & Jimenez-Ibarra et al. 2019). Research has found that the winds from hot accretion flows are emitted and accelerated under the combined action of centrifugal force, gas pressure gradient and magnetic pressure gradient (Yuan et al. 2012; Yuan et al. 2015; Narayan et al. 2012; Bu & Gan 2018).

For the case of the cold accretion mode, it is associated with a relatively high mass accretion rate and comprised of cool optically thick gas. Observational evidences of the winds from cold thin disks have been reported for luminous AGNs

(Crenshaw et al. 2003; Tombesi et al. 2010; Tombesi et al. 2014; Liu et al. 2013; Gofford et al. 2015; King & Pounds 2015; He et al. 2019) and the soft state of black hole X-ray binaries (Neilsen & Homan 2012; Díaz Trigo & Boirin 2016; Homan et al. 2016; You et al. 2016).

Theoretically, there are three important mechanisms, namely the thermal driving, magnetic driving, and radiation line force driving, which are believed to accelerate the disk winds for a cold standard thin disk. The thermal driving mechanism can commendably understand the winds observed in some low-mass X-ray binaries (Begelman et al. 1983; Woods et al. 1996; Higginbottom et al. 2017). The magnetic driving mechanism can effectively explain the winds in many astrophysical environments (Blandford & Payne 1982; Cao 2014). The radiation line force driving is a compelling mechanism to interpret the ionization state of the winds and understand fast outflows and ultra-fast outflows (UFOs) (Proga et al. 2000; Nomura et al. 2016; Nomura & Ohsuga 2017; Yang et al. 2021).

For the radiation line force driving mechanism, if the gas is moderately ionized and can interact with the UV continuum through many UV line transitions, the radiation pressure force due to spectral lines (i.e., line force) would accelerate the matter and launch the cold winds. The line force can be 1000 times larger than the radiation pressure force due to Thomson scattering (Stevens & Kallman 1990; Liu et al. 2013), and leads to high-velocity disk winds. Hydrodynamic simulations of winds driven by the line force have been implemented (Proga et al. 2000; Proga & Kallman 2004; Nomura et al. 2016; Nomura & Ohsuga 2017; Nomura et al. 2020; Yang et al. 2021). It is found

that the line force can effectively drive high speed winds from the inner region of a cold thin accretion disk and the UFOs (Tombesi et al. 2010) are commendably explained by line-driven disk wind model. Yang (2021b) perform two-dimensional magnetohydrodynamic (MHD) simulations to understand the formation and acceleration of UFOs in radio-loud AGNs. Higher-velocity winds with a broader opening angle are produced in their MHD models and UFOs in radio-loud AGNs may be driven by the combination of line force and magnetic field. Ajello et al. (2021) study gamma-rays from fast black hole winds. They find that these outflows transfer 0.04 % of their mechanical power to γ -rays and the γ -ray emission is from galaxies with UFOs.

In order to know the propagation and the properties of the winds at large scale (around parsec scale), Cui et al. (2020); Cui & Yuan (2020b) study the large-scale dynamics of the winds through simulation and analytical methods. They find that when the winds from a cold thin disk have a negative Bernoulli parameter, the winds will only propagate a short distance from their simulated injection inner boundary. However, they neglect the radiation force in their simulations. Zhu et al. (2022) include both radiation force and radiative cooling/heating and perform numerical simulations to study the large scale dynamics of winds. They indicate that the properties of the winds depend on the mass of black hole and the luminosity of accretion disk.

However, all the above mentioned radiation driven winds simulations only consider the radiation force due to electron scattering and UV line processes due to the first order radiation coming from the central AGNs. They neglect the scattered and reprocessed photons. In reality, the locally generated photons through scattering, bremsstrahlung and line radiation in the gas around parsec scale can also play an important role. The radiation force due to the locally generated photons is called the re-radiation force and the resulting impact corresponds to the re-radiation effect.

Sim et al. (2010) study multi-dimensional radiative transfer simulation to calculate the spectrum of the hydrodynamics simulation of the line-driven accretion disk winds. They find that the secondary photons ionize the winds materials. Higginbottom et al. (2014) perform Monte Carlo simulations of the radiative transfer. It is found that scattered photons can also ionize gases, resulting in excessively high levels of ionization. However, the postprocess approach, which is decoupling radiative transfer and HD/MHD calculations, is implemented in their works. Liu et al. (2013) investigate the effect of re-radiation force on the dynamics of the flows at parsec scale under the irradiation from the central AGNs. They find that the accretion flows properties change significantly due to the re-radiation effect and outflows become stronger consequently. Mosallanezhad et al. (2019) improve the calculation of radiation force due to local process and make comparison between total radial directions forces and

re-radiation forces. They find that the mass flux and velocity of the outflows are significantly increased and the outflows are mainly driven by the re-radiation force. Obviously, the re-radiation effect has an important impact on the accretion flows at large scale. However, those simulations concentrate only on the large scale of the accretion flows, and they do not consider the accelerating of the matter in the inner scale due to the line force. Substantial radiative accelerations occur within small scale and even lead to high-velocity (0.1–0.2c) disk winds (Proga et al. 2000; Proga & Kallman 2004; Nomura et al. 2016; Nomura & Ohsuga 2017). They will exchange their momentum and energy with the gas. When the winds arrive at parsec scale, thus, it is interesting to study the dynamics of the winds driven by the combination of radiation line force and re-radiation force.

In the paper, we conduct numerical simulations to investigate the large scale dynamics of winds driven by the line force and the re-radiation force. In our simulations, radiation line force, re-radiation force, and radiative cooling/heating are all included. We first simulate small scale winds driven the radiation line force in a dynamical range of 30–1500 r_s and the time-averaged properties of winds. Then, we perform our large scale simulations in a dynamic range of 1500–10⁶ r_s . We concentrate on the large scale dynamic of the winds driven by the line force and the re-radiation force. The aim of carrying out small scale simulations is to derive internal boundary conditions for the large scale simulations. Winds are injected into the inner boundary of large scale simulations. The properties of the injected winds come from the time-averaged value of winds at outer boundary of the small scale simulations.

The paper is organized as follows: Section 2 describes our models and methods; Section 3 introduces our results; Section 4 gives discussions, and a summary is presented in Section 5.

2. Model and Method

We perform axisymmetric two-dimensional radiation hydrodynamic simulations by PLUTO code, which solves systems of conservation laws using the finite volume or finite difference approach based on Godunov-type schemes (Mignone et al. 2007; Mignone et al. 2012; Yang et al. 2021; Yang 2021b; Zhu et al. 2022). The basic scenario and physical setup of our models are mostly the same as one used in Zhu et al. (2022).

2.1. Basic Equations

We carry out two-dimensional numerical hydrodynamic simulations. The spherical coordinates (r, θ, ϕ) are employed and the equations are solved as follows

$$\frac{d\rho}{dt} + \rho \nabla \cdot \mathbf{v} = 0, \quad (1)$$

$$\rho \frac{d\mathbf{v}}{dt} = -\nabla P - \rho \nabla \Phi + \rho \mathbf{F}_{\text{rad}}, \quad (2)$$

$$\rho \frac{d}{dt} \left(\frac{e}{\rho} \right) = -P \nabla \cdot \mathbf{v} + \rho \zeta. \quad (3)$$

Here, ρ , \mathbf{v} , P , e , ζ and Φ are density, velocity, gas pressure, internal energy, the net cooling/heating rate and gravitational potential, respectively. \mathbf{F}_{rad} is the radiation force per unit mass including Compton scattering, line force, and re-radiation force. We apply an equation of state of ideal gas $P = (\gamma - 1)e$ with $\gamma = 5/3$. In this work, we consider the gravitational potential of both the central black hole $\Phi_{\text{BH}} = -GM_{\text{BH}}/(r - r_s)$ (Paczynski & Wiita 1980) and the host galaxy $\Phi_{\text{Galaxy}} = \sigma_v \ln r + C$ (Dye et al. 2008; Bu et al. 2016; Cui et al. 2020), where M_{BH} , G , r_s , r , C and σ_v are the mass of black hole, the gravitational constant, the Schwarzschild radius, the distance from a point to the black hole, the constant, and the velocity dispersion, respectively. We adopt the velocity dispersion $\sigma_v = 2 \times 10^7 \text{ cm s}^{-1}$.

2.2. Model Setup

It is assumed that a geometrically thin and optically thick disk is around the central black hole for luminous AGNs. The thin disk is responsible for the UV emissions and the hot corona is responsible for the X-ray emissions. The hot corona can irradiate the thin disk, and the radiation intensity from the surface of the accretion disk is written as

$$I_{\text{D}}(r_{\text{D}}) = \frac{3GM_{\text{BH}}\dot{M}_a}{8\pi^2 r_*^3} \left(\frac{r_*}{r_{\text{D}}} \right)^3 \left[1 - \left(\frac{r_*}{r_{\text{D}}} \right)^{1/2} \right] + \frac{f_x}{3\pi} \left\{ \arcsin \frac{r_*}{r_{\text{D}}} - \frac{r_*}{r_{\text{D}}} \left[1 - \left(\frac{r_*}{r_{\text{D}}} \right)^2 \right]^{1/2} \right\}. \quad (4)$$

Here, r_{D} , r_* and \dot{M}_a denote the radial position on the disk surface measured from the central black hole, the inner edge of the disk, and the mass accretion rate of the accretion disk, respectively. f_x is the ratio of the X-ray luminosity L_X from the corona to the disk luminosity L_{D} ($f_x = L_X/L_{\text{D}}$). We refer to Yang et al. (2021) for the detailed calculation of the value of f_x . The effective temperature of the disk surface is determined by $T_{\text{eff}} = (\pi I_{\text{D}}(r_{\text{D}})/\sigma)^{1/4}$, with σ being the Stefan-Boltzmann constant. We consider that the radiation from the high-temperature ($>3000\text{K}$) region of the accretion disk contributes to the line force.

The gas above the accretion disk is irradiated by the UV photons from the accretion disk surface and the X-ray photons from the corona. Our simulations are implemented in a spherical coordinate (r, θ, φ) . We put the surface of the accretion disk on the plane of $\theta = \pi/2$. The plane of $\theta = \pi/2$ is above the equatorial plane, at the height z , corresponding to the disk scale height. For simplicity of calculation, we assume that

the disk scale height is a constant of radius ($z = 3.1\epsilon r_s$, with ϵ being the Eddington ratio, Nomura & Ohsuga 2017).

The line force and the force multiplier \mathbf{M} , depend on the ionization of the winds and the spectral energy distribution of the radiation field. For more details of the calculations, readers are referred to Proga et al. (1998) and Proga et al. (2000).

We assume that initially the gas above the thin disk is in hydrostatic equilibrium ($\rho'(r, \theta) = \rho'(\pi/2)\exp(-\frac{GM_{\text{BH}}}{2c_s^2 r \tan^2 \theta})$) and locally isothermal ($T(r, \theta) = T_{\text{eff}}(r \sin \theta)$) in small scale simulations. The density of the surface of the accretion disk $\rho'(\pi/2)$ is set according to the standard thin disks model (Shakura & Sunyaev 1973; Nomura & Ohsuga 2017). For the large scale simulations, we do not consider an accretion disk at the midplane. Our computational domain covers from $1500r_s$ to $1.5 \times 10^6 r_s$. We employ non-uniform grids to discretize the computational domain. Our resolution is 300×160 . Initially, low density gas ρ_0 is put in the computational domain. Note, various ρ_0 , ϵ and M_{BH} are adopted. The details of various models are listed in Table 1. We employ axis-of-symmetry boundary conditions at $\theta = 0^\circ$ and adopt equator-of-symmetry boundary conditions at $\theta = 90^\circ$. Refer to Zhu et al. (2022) for more details on computational domain and boundary conditions.

2.3. Radiative Cooling/heating

The radiative processes and the interaction between the radiation include Compton heating/cooling, X-ray photoionization and recombination, bremsstrahlung, and line cooling (Blondin 1994; Proga et al. 2000). The net cooling rate ζ denotes as follows

$$\rho \zeta = n^2 (G_{\text{Compton}} + G_X - L_{b,l}), \quad (5)$$

where n is the number density,

$$n = \rho/\mu m_p, \quad (6)$$

G_{Compton} is the rate of Compton heating/cooling,

$$G_{\text{Compton}} = 8.9 \times 10^{-36} \zeta (T_X - 4T), \quad (7)$$

G_X is the net rate of X-ray photoionization heating-recombination cooling,

$$G_X = 1.5 \times 10^{-21} \zeta^{1/4} T^{-1/2} (1 - T/T_X), \quad (8)$$

and $L_{b,l}$ is the rate of bremsstrahlung and line cooling,

$$L_{b,l} = 3.3 \times 10^{-27} T^{1/2} + [1.7 \times 10^{-18} \times \exp(-1.3 \times 10^5/T) \times \zeta^{-1} T^{-1/2} + 10^{-24}] \delta. \quad (9)$$

In the above equations, $\mu = 1$ denotes the mean molecular weight, m_p is the proton mass, and $T_X = 10^8 \text{ K}$ is the characteristic temperature of the X-ray radiation. The parameter δ is used to control line cooling. We set $\delta = 1$, which represents optically thin cooling.

Table 1
 Summary of Models

| Model numbers (1) | Cold Disk Winds (2) | Potential (3) | Re-Radiation (4) | M_{BH} (M_{\odot}) (5) | ϵ (6) | ρ_0 (g cm^{-3}) (7) |
|----------------------|---------------------------|------------------|---------------------|---|-------------------|---|
| 1 | <i>RHD86_bh_d</i> | <i>bh</i> | <i>no</i> | 10^8 | 0.6 | $2.25 \times 10^{-14} r_s^2 / r^2$ |
| 2 | <i>RHD86_bh + g_d</i> | <i>bh + g</i> | <i>no</i> | 10^8 | 0.6 | $2.25 \times 10^{-14} r_s^2 / r^2$ |
| 3 | <i>RERHD86_bh + g_d</i> | <i>bh + g</i> | <i>yes</i> | 10^8 | 0.6 | $2.25 \times 10^{-14} r_s^2 / r^2$ |
| 4 | <i>RHD86_bh + g_d25</i> | <i>bh + g</i> | <i>no</i> | 10^8 | 0.6 | 10^{-25} |
| 5 | <i>RERHD86_bh + g_d25</i> | <i>bh + g</i> | <i>yes</i> | 10^8 | 0.6 | 10^{-25} |
| 6 | <i>RHD86_bh + g_d23</i> | <i>bh + g</i> | <i>no</i> | 10^8 | 0.6 | 10^{-23} |
| 7 | <i>RERHD86_bh + g_d23</i> | <i>bh + g</i> | <i>yes</i> | 10^8 | 0.6 | 10^{-23} |
| 8 | <i>RHD63_bh_d</i> | <i>bh</i> | <i>no</i> | 10^6 | 0.3 | $2.25 \times 10^{-14} r_s^2 / r^2$ |
| 9 | <i>RHD63_bh + g_d</i> | <i>bh + g</i> | <i>no</i> | 10^6 | 0.3 | $2.25 \times 10^{-14} r_s^2 / r^2$ |
| 10 | <i>RERHD63_bh + g_d</i> | <i>bh + g</i> | <i>yes</i> | 10^6 | 0.3 | $2.25 \times 10^{-14} r_s^2 / r^2$ |
| 11 | <i>RHD63_bh + g_d25</i> | <i>bh + g</i> | <i>no</i> | 10^6 | 0.3 | 10^{-25} |
| 12 | <i>RERHD63_bh + g_d25</i> | <i>bh + g</i> | <i>yes</i> | 10^6 | 0.3 | 10^{-25} |
| 13 | <i>RHD63_bh + g_d23</i> | <i>bh + g</i> | <i>no</i> | 10^6 | 0.3 | 10^{-23} |
| 14 | <i>RERHD63_bh + g_d23</i> | <i>bh + g</i> | <i>yes</i> | 10^6 | 0.3 | 10^{-23} |

| Model numbers (1) | Cold disk winds (2) | \dot{M}_W ($10L_{\text{edd}}/c^2$) (8) | \dot{P}_W (L_{edd}/c) (9) | \dot{E}_W (L_{edd}) (10) |
|----------------------|---------------------------|--|--|---|
| 1 | <i>RHD86_bh_d</i> | 0.11377 | 0.14548 | 0.021582 |
| 2 | <i>RHD86_bh + g_d</i> | 0.11372 | 0.14542 | 0.021574 |
| 3 | <i>RERHD86_bh + g_d</i> | 0.11372 | 0.14552 | 0.021606 |
| 4 | <i>RHD86_bh + g_d25</i> | 0.11805 | 0.14605 | 0.021522 |
| 5 | <i>RERHD86_bh + g_d25</i> | 0.11889 | 0.14486 | 0.021557 |
| 6 | <i>RHD86_bh + g_d23</i> | 0.76886 | 0.55599 | 0.061511 |
| 7 | <i>RERHD86_bh + g_d23</i> | 0.96922 | 0.78302 | 0.079268 |
| 8 | <i>RHD63_bh_d</i> | 1.8611×10^{-7} | 1.4586×10^{-8} | 1.4797×10^{-10} |
| 9 | <i>RHD63_bh + g_d</i> | 1.8585×10^{-7} | 1.3447×10^{-8} | 1.2835×10^{-10} |
| 10 | <i>RERHD63_bh + g_d</i> | 2.6390×10^{-7} | 3.8471×10^{-8} | 7.7709×10^{-10} |
| 11 | <i>RHD63_bh + g_d25</i> | 3.2168×10^{-10} | 9.1662×10^{-13} | 2.9331×10^{-16} |
| 12 | <i>RERHD63_bh + g_d25</i> | 8.3898×10^{-10} | 4.0696×10^{-12} | 2.3195×10^{-15} |
| 13 | <i>RHD63_bh + g_d23</i> | 3.2534×10^{-9} | 1.5052×10^{-12} | 6.9671×10^{-16} |
| 14 | <i>RERHD63_bh + g_d23</i> | 4.6444×10^{-8} | 7.9759×10^{-12} | 4.5078×10^{-15} |

Note. Column (1): model numbers; column (2): model names; column (3): the gravitational potential; column (4): the radiation force (whether the re-radiation force is included); column (5): the mass of the black hole; column (6): the Eddington ratio ($\epsilon = L_D/L_{\text{edd}}$); column (7): the initial density of computational domain. Column (1): model numbers; column (2): model names; column (8)–(10) are the time-averaged mass outflow fluxes, momentum fluxes and kinetic energy fluxes of the winds measured at the outer radial boundary ($r = 1.5 \times 10^6 r_s$), respectively.

The net cooling rate ζ depends on the density ρ , the temperature T , the characteristic temperature of the X-ray radiation T_X , and the ionization parameter ξ . Here, the ionization parameter ξ is expressed as

$$\xi = \frac{f_x L_D}{nr^2} \exp(-\tau_X), \quad (10)$$

where τ_X is the optical depth for the X-ray from the corona. For the large scale simulations, we calculate the optical depth for the X-ray τ_X from the corona and the optical depth for the UV radiation τ_{UV} from the accretion disk as follows

$$\tau_X(r, \theta) = \tau_{0,X} + \int_{1500r_s}^r \sigma_X \rho(r', \theta) dr', \quad (11)$$

$$\tau_{\text{UV}}(r, \theta) = \tau_{0,\text{UV}} + \int_{1500r_s}^r \sigma_e \rho(r', \theta) dr'. \quad (12)$$

where $\tau_{0,X}$, $\tau_{0,\text{UV}}$ are the optical depths for the X-ray and the UV radiation respectively across the entire domain of the small scale simulations, σ_e is the mass-scattering coefficient for free electrons and set to be $0.4 \text{ g}^{-1} \text{ cm}^2$. We set $\sigma_X = \sigma_e$ for $\xi \geq 10^5 \text{ erg cm s}^{-1}$ and $\sigma_X = 100\sigma_e$ for $\xi < 10^5 \text{ erg cm s}^{-1}$ (Proga et al. 2000; Yang et al. 2021).

2.4. The Radiation Force

Liu et al. (2013) and Mosallanezhad et al. (2019) indicate that the re-radiation effect can significantly affect the properties

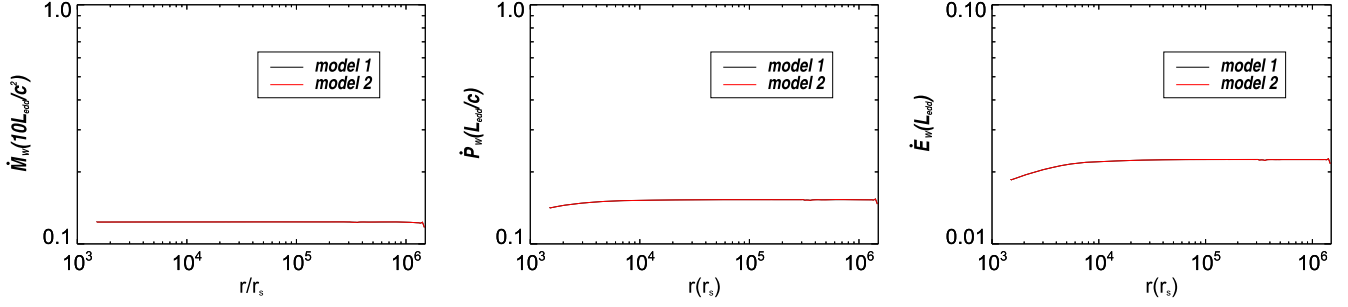


Figure 1. Time-averaged mass fluxes (left panel), momentum fluxes (middle panel) and kinetic power (right panel) of winds for models 1 and model 2. The curves of model 1 and 2 are overlapped.

of the accretion flow around parsec scale. Therefore, the re-radiation force can play an important role in driving winds process when the winds spread to large scale, which launch from inside hundreds of Schwarzschild radius.

The total radiation force includes the radiation force F_r^c from the center AGNs and the re-radiation force F_z^{re} due to the locally produced photons,

$$F_{\text{rad}} = F_r^c + F_z^{\text{re}}. \quad (13)$$

Here, the re-radiation force F_z^{re} is in the z-direction, and is described by

$$F_z^{\text{re}} = \int_0^z (S_c + n^2 l_{b,l}) dz \hat{z}, \quad (14)$$

where

$$S_c = \rho \sigma_e (F_D + F_X), \quad (15)$$

is the source term and it denotes the first-order scattered photons of the radiation from the central AGNs (Liu et al. 2013). F_D and F_X are the accretion disk flux and the X-ray flux, respectively.

The radiation force F_r^c from the center AGNs is expressed as

$$F_r^c = \frac{n^2 G_X}{\rho c} + \frac{\sigma_e}{c} (1 + M) F_D \hat{r} + \frac{\sigma_e}{c} F_X \hat{r}. \quad (16)$$

In the above equation, the first term on the right-hand side is the force corresponding to photoionization heating-recombination cooling $F_r^{c,\text{ph}}$ (Liu et al. 2013), the second term denotes the force for the UV radiation $F_r^{c,\text{line}}$, which corresponds to Thomson scattering and line force, and the third term denotes the force for the X-ray radiation $F_r^{c,x}$. We note that the simplification of radiation force from X-ray photoionization heating and recombination cooling will underestimate the force and this approximation is feasible because of the radiation force in the radial direction being in general dominated by the line force.

There is a difference here in the calculation of the accretion disk flux F_D : we calculate it by the specific vector-valued integral (Proga et al. 1998, 2000), while Mosallanezhad et al. (2019) adopt point-source approximation. Although the point-source approximation approach is feasible around parsec scale,

the vector-valued integral is more accurate and reliable in our simulations. In the paper, F_D and F_X are obtained as follows

$$F_D = \int I_D(r_D) \mathbf{n} d\Omega, \quad (17)$$

$$F_X = \frac{f_x L_D}{4\pi r^2}, \quad (18)$$

where \mathbf{n} is the unit vector, and Ω is the solid angle subtended by the disk and central object.

3. Results

We perform simulations with different values of initial gas density ρ_0 and accretion disk luminosity $L_D = \varepsilon L_{\text{edd}}$ (L_{edd} being Eddington luminosity) to explore the re-radiation effect of these parameters. In the paper, we also study the influence of galactic potential on the dynamics of the winds. The model parameters and the general results are summarized in Table 1. The properties of the winds in Table 1 are obtained by time-averaging the values at the outer radial boundary. We give the time-averaged values on time interval of $0.5T_{\text{ob}} - 1.0T_{\text{ob}}$, where T_{ob} denotes the orbital time at the radial outer boundary.

3.1. The Effect of the Host Galaxy Potential

Model 1 and model 2 show the winds without and with galaxy potential for $M_{\text{BH}} = 10^8 M_{\odot}$, $\varepsilon = 0.6$, respectively. In Figure 1, we plot the time-averaged mass fluxes, momentum fluxes and kinetic power of the winds for model 1 and model 2. The mass outflow flux, momentum flux and kinetic energy flux are calculated as follows

$$\dot{M}_w(r) = 4\pi r^2 \int_{0^\circ}^{89^\circ} \rho \max(v_r, 0) \sin \theta d\theta, \quad (19)$$

$$\dot{P}_w(r) = 4\pi r^2 \int_{0^\circ}^{89^\circ} \rho \max(v_r^2, 0) \sin \theta d\theta, \quad (20)$$

$$\dot{E}_w(r) = 4\pi r^2 \int_{0^\circ}^{89^\circ} \frac{1}{2} \rho \max(v_r^3, 0) \sin \theta d\theta. \quad (21)$$

In the two models, the mass fluxes keep almost unchanged with radius and the momentum fluxes and kinetic power

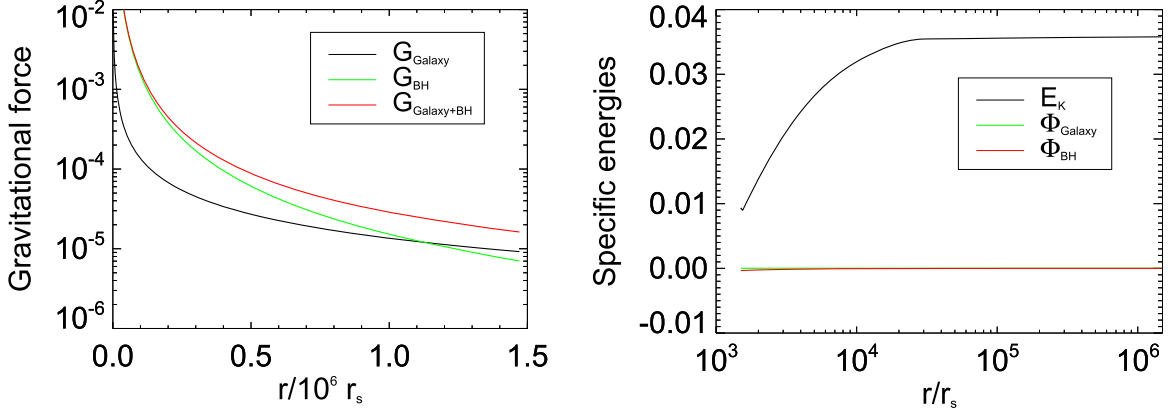


Figure 2. Left panel: distribution of specific gravitational force with radius (black line, green line and red line correspond to the gravitational force of galaxy, black hole and their sum, respectively). Right panel: the r dependence of time-averaged kinetic energy along $\theta = 71^\circ$ ($1/2(v/c)^2$, black line), galaxy gravitational energy ($\sigma_v^2 \ln r/c^2$, green line) and black hole gravitational energy ($GM_{\text{BH}}/(r - r_s)c^2$, red line) for model 2.

increase due to the acceleration by line force. The winds do not stop at the outer radial boundary of our simulations and can move out of the AGNs to interact with the interstellar medium of their host galaxies. The kinetic power of the winds is significantly higher than $0.5\% L_{\text{edd}}$, so the winds can provide sufficient feedback to their host galaxies (Di Matteo et al. 2005; Hopkins & Elvis 2010; Bu & Yang 2021). It is clear that the curves of the mass flux, momentum flux and kinetic power are almost same for model 1 and model 2. This indicates that including the gravitational potential of host galaxy has little impact on the large-scale dynamics of the winds.

The left panel in Figure 2 shows the r dependence of the specific gravitational force. The black hole gravitational force dominates the gravitational force for $r < 1.1 \times 10^6 r_s$, while the host galaxy gravitational force dominates for $r > 1.1 \times 10^6 r_s$. The total gravitational force is same with the gravitational force due to the black hole when $r < 10^5 r_s$. The right panel in Figure 2 shows time-averaged kinetic energy of winds along $\theta = 71^\circ$ (at this angle, the winds move almost radially), galaxy gravitational energy, and black hole gravitational energy. It is clear that the kinetic energy of the winds is significantly larger than their galaxy gravitational energy and black hole gravitational energy, especially when $r > 10^5 r_s$. Therefore, the galaxy gravitational energy and the black hole gravitational energy can be negligible compared to the kinetic energy. Thus, there is little effect on the large-scale dynamics of the winds for including the host galaxy potential.

We also study the effect of the host galaxy potential for various accretion disk luminosity. From Table 1, as we can see that compared to model 8, in model 9, the mass flux at the outer boundary slightly decrease and momentum flux and kinetic energy flux reduce to about 90%. This indicates that the host galaxy potential works and restrains the outflows for $M_{\text{BH}} = 10^6 M_\odot$, $\varepsilon = 0.3$. The reasons are as follows. The kinetic

energy of the winds is rather small and the winds cannot reach the outer boundary for the case of $M_{\text{BH}} = 10^6 M_\odot$, $\varepsilon = 0.3$. Moreover, the black hole gravitational energy decreases compared to model 1 and model 2. Thus the effect with inclusion of the galaxy potential is more obvious. However, those fluxes measured at the outer boundary are significantly small and the winds cannot escape from gravitational potential.

3.2. The Fiducial Run

We choose model 3 as the fiducial model in our paper and compare it with model 2. The parameters of the fiducial model are $M_{\text{BH}} = 10^8 M_\odot$, $\varepsilon = 0.6$, $\rho_0(r) = 2.25 \times 10^{-14} r_s^2 / r^2$. Obviously, the fiducial model involves the host galaxy potential and the re-radiation force. The only difference between model 3 and model 2 lies whether the re-radiation force is included.

In Figure 3, we plot some snapshots of density (color) and velocity (arrows) for model 2 and model 3. The upper panels correspond to $t = 0.1 T_{\text{ob}}$ and the bottom panels correspond to $t = 0.5 T_{\text{ob}}$. The right panels are for model 2, while the left panels are for model 3. The winds go away in the direction of $\theta = 71^\circ$. From $t = 0.1 T_{\text{ob}}$ to $t = 0.5 T_{\text{ob}}$, it can be seen that the winds spread to the outer boundary and the radial speed of the winds is continuously increased. This means that the accretion disk winds driven by the radiation mechanism move outwards and even can go to outside $1.5 \times 10^6 r_s$. Comparing the upper right panel of Figure 3 to the upper left panel, we can see that the velocity of the winds in model 3 is slightly larger than that of the winds in model 2. Hence, the distance of winds propagation for model 3 is further. The gas density close to the equatorial plane decreases. Comparing the bottom right panel to the bottom left panel, we can see that the velocity and density of the winds in model 3 are almost the same with the velocity and density in model 2. This indicates that the re-

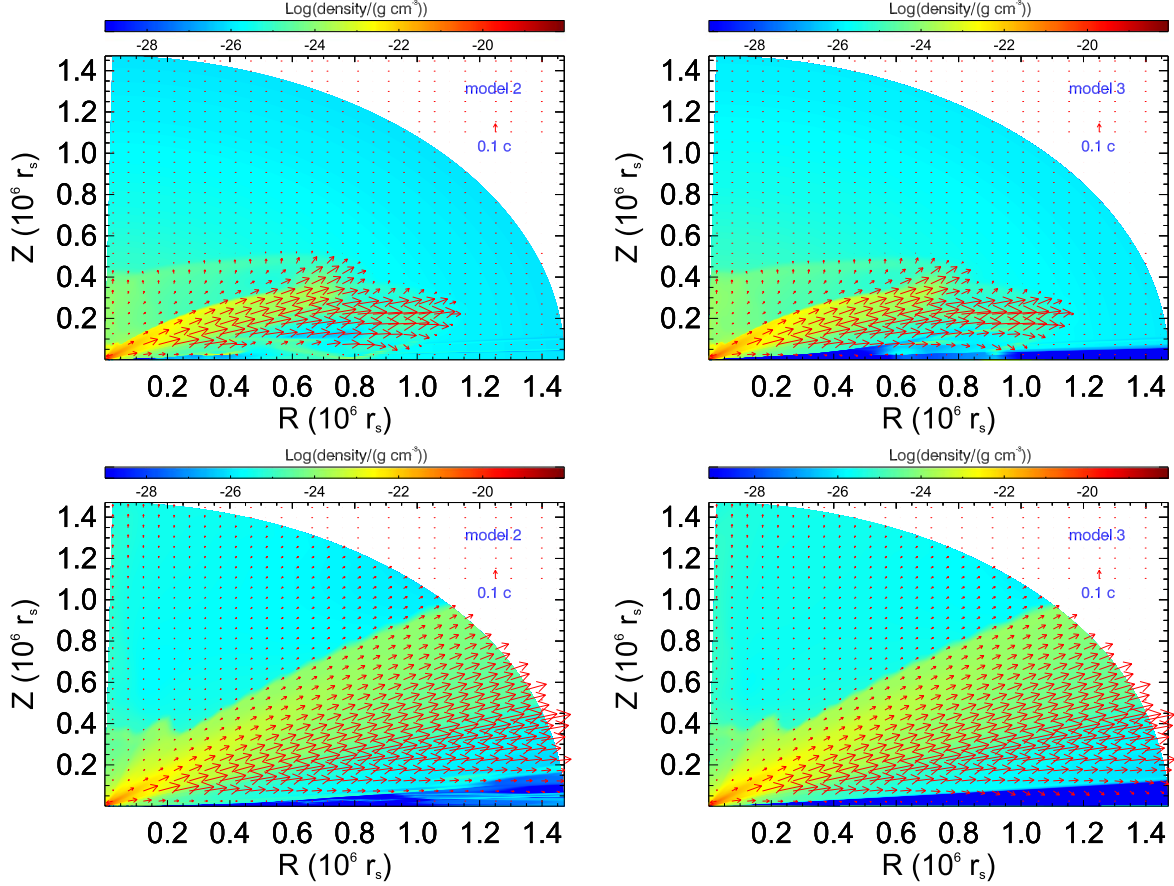


Figure 3. Comparison between models 2 and model 3. Top left: snapshot of density (color) and velocity (arrows) at $t = 0.1T_{\text{ob}}$ for model 2. Top right: snapshot of density (color) and velocity (arrows) at $t = 0.1T_{\text{ob}}$ for model 3. Bottom left: snapshot of density (color) and velocity (arrows) at $t = 0.5T_{\text{ob}}$ for model 2. Bottom right: snapshot of density (color) and velocity (arrows) at $t = 0.5T_{\text{ob}}$ for model 3.

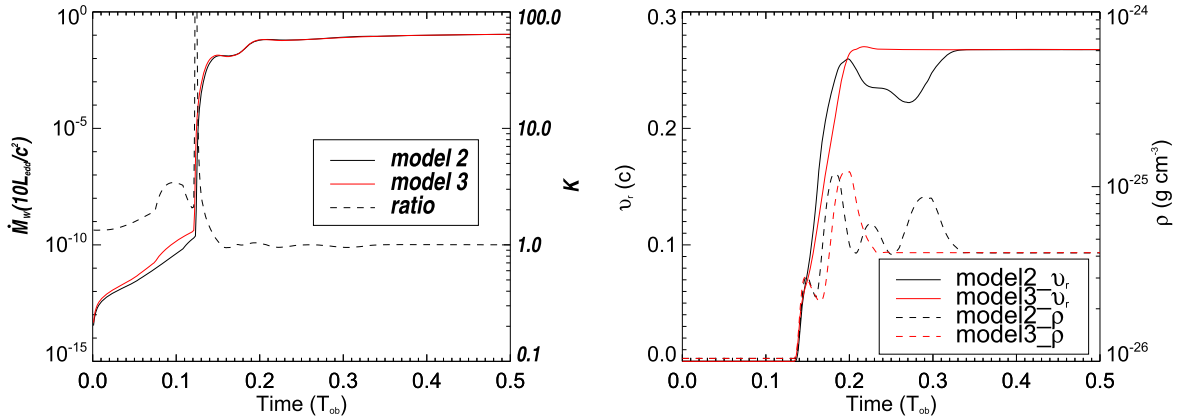


Figure 4. Properties of the outflows from 0 to $0.5T_{\text{ob}}$ for model 2 and model 3. Left panel: time dependence of the mass fluxes of outflows measured at $1.5 \times 10^6 r_s$ (solid black line for model 2, solid red line for model 3) and the mass flux ratio K (dashed line). Right panel: time dependence of radial velocities (solid black line for model 2, solid red line for model 3) and densities (dashed black line for model 2, dashed red line for model 3). The radial velocities and densities are measured at $r = 1.5 \times 10^6 r_s$, $\theta = 71^\circ$. The ordinate on the left-hand side refers to the solid line, while the ordinate on the right-hand side refers to the dashed line.

radiation force drives stronger outflows at the first and after a period of time the re-radiation effect could be almost negligible. In order to show this point more clearly, we plot the properties of the winds from 0 to $0.5 T_{\text{ob}}$ for model 2 and model 3 in Figure 4.

The left panel of Figure 4 shows the mass outflow fluxes of winds (solid black line for model 2, solid red line for model 3) on the range of $0-0.5T_{\text{ob}}$. It is clear that the mass flux for model 3 is larger than that for model 2 from 0 to $0.12 T_{\text{ob}}$. After a period of time (about $0.15T_{\text{ob}}$), the mass flux for model 3 is same with that for model 2. The dashed line of the left panel in Figure 4 shows the mass flux ratio K (the ratio of the mass flux for model 3 to that for model 2). It can be seen that the mass flux ratio is larger than 1 from 0 to $0.16T_{\text{ob}}$ and almost equals to 1 from $0.2T_{\text{ob}}$ to $0.5T_{\text{ob}}$. The right panel of Figure 4 shows time dependence of radial velocity (solid black line for model 2, solid red line for model 3) and density (dashed black line for model 2, dashed red line for model 3) at $r = 1.5 \times 10^6 r_s$, $\theta = 71^\circ$. It is seen that the velocity and density of the outflows have a sharp increase at $0.13T_{\text{ob}}$. The velocity and density of the outflows for model 3 start to keep steady at $0.23T_{\text{ob}}$, and the outflows for model 2 maintain a quasi-steady state at $0.34T_{\text{ob}}$. When the quasi-steady is formed, the properties of the outflows are same for model 2 and model 3. As Mosallanezhad et al. (2019) found, the outflows rate of the accretion flows at the outer boundary is enhanced under the irradiation from the central AGNs when we include the re-radiation force. The re-radiation force works and plays an important role in the early stage. Thus, the mass flux for model 3 is larger than that for model 2 from 0 to $0.16 T_{\text{ob}}$ and even two orders of magnitude larger than the mass flux for model 2 at $0.12T_{\text{ob}}$. However, the value of the mass flux is extremely small during this period. After the quasi-steady state being formed, the winds are driven by the combination of line force and re-radiation force and the UV radiation due to spectral lines dominates total radiation in the simulations. Therefore, the mass flux, velocity and density of model 2 and model 3 are almost the same. To prove this point, we plot Figure 5.

Figure 5 shows the structure of time-averaged radiation fluxes in units of coef for model 3. The left columns give the time-averaged radiation fluxes ($F_r^{c,\text{phx}}$, $F_r^{c,\text{line}}$) in the radial direction and the right columns give time-averaged radiation fluxes (F_z^{re} , F_z^{line}) in the vertical direction. Comparing the upper left panel to the middle left panel of this figure, we can see that the value of time-averaged radiation flux $F_r^{c,\text{line}}$ due to the UV radiation from the AGNs in the radial direction is much greater than the value of radiation flux $F_r^{c,\text{phx}}$ due to photoionization heating-recombination cooling and X-ray radiation. To specify this statement, we plot the bottom left panel of this figure, which shows the distribution of the radiation fluxes with radius. It is clear that $F_r^{c,\text{line}}$ is almost eight orders magnitude larger than $F_r^{c,\text{phx}}$ along $\theta = 71^\circ$. This indicates that radiation flux due

to photoionization heating-recombination cooling and X-ray radiation can almost be neglected and the UV radiation dominates total radiation in the radial direction when the flows get into the steadiness.

Comparing the upper right panel to the middle right panel of Figure 5, it is seen that the time-averaged value of radiation flux F_z^{line} due to the UV radiation from the central AGNs in the vertical direction is much greater than the radiation flux F_z^{re} due to the local photons from the local radiative processes and scattered photons. From the bottom right panel of this figure, we can see that F_z^{line} is almost nine orders magnitude larger than F_z^{re} along $\theta = 71^\circ$. Thus, the radiation flux due to the local photons from the local radiative processes and scattered photons can nearly be ignored and the re-radiation effect is almost negligible for $M_{\text{BH}} = 10^8 M_\odot$, $\varepsilon = 0.6$ when the quasi-steady state has been formed. Therefore, the properties of the winds are almost the same. The kinetic power of the winds is significantly higher than $0.5\% L_{\text{edd}}$ and the winds can provide sufficient feedback to their host galaxies. There are deep red areas within $10^5 r_s$ in the middle panels of Figure 5 and bulges within $3 \times 10^4 r_s$ (red line) in the bottom panels. The sharp increases are due to the line force multiplier \mathbf{M} . As Zhu et al. (2022) found, the winds are accelerated when they move from small to large radii inside $10^5 r_s$, and the line force multiplier \mathbf{M} is negligibly small outside $\sim 10^5 r_s$. We note, compared with the work of Mosallanezhad et al. (2019), the re-radiation force seems unimportant due to the low initial gas density.

3.3. Initial Gas Density Dependence

We study the effect of initial gas density (ρ_0) in this section. Figure 6 shows the comparison of properties of the winds for models 3, 5 and 7. From the top left panel, top right panel to bottom left panel, we can see that the densities, in the region ($\theta < 45^\circ$), are increased. The densities and the velocities of the winds, in the region ($\theta > 60^\circ$), are the same. In addition, the velocities of the winds in the region ($45^\circ < \theta < 60^\circ$) are decreased. This means that the opening angle of winds is getting narrower and narrower. To show this point clearly, we plot the bottom right panel of Figure 6. The bottom right panel shows angular distribution of the winds densities and velocities at outer boundary for models 3, 5 and 7. It can be seen that the densities for models 3, 5 and 7 in the region ($\theta < 45^\circ$) nearly maintain at the level of about $10^{-26} \text{ g cm}^{-3}$, $10^{-25} \text{ g cm}^{-3}$ and $10^{-23} \text{ g cm}^{-3}$, respectively. The densities at outer boundary exactly correspond to their initial densities. In the region ($45^\circ < \theta < 60^\circ$), the densities and velocities change with angle and finally each tend to be consistent. In the region ($60^\circ < \theta < 80^\circ$), the curves of densities are the same, so are the velocities curves. The reasons are as follows. The winds go away in the angle of $45^\circ < \theta < 80^\circ$ for $M_{\text{BH}} = 10^8 M_\odot$, $\varepsilon = 0.6$. So models 3, 5 and 7 in the region ($\theta < 45^\circ$) have few velocities and the densities are almost equal to their initial

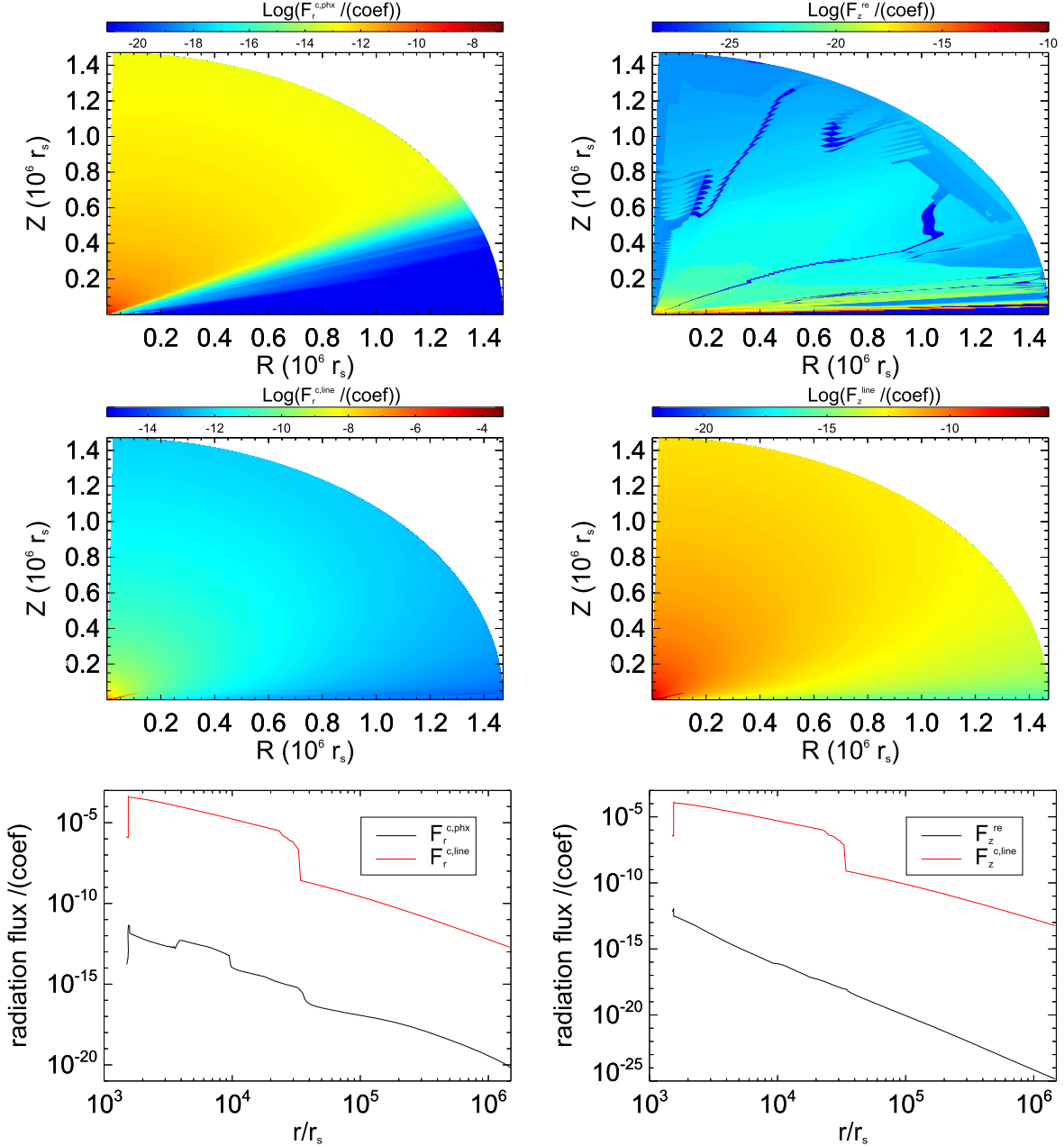


Figure 5. Structure of radiation flux in units of coef ($\text{coef} = 3\sigma_e GM_{\text{BH}} \dot{M}_a / 4\pi^2 cr_*^3$) for model 3. Top left: time-averaged radiation flux $F_r^{c,\text{phx}}$ due to photoionization heating-recombination cooling and X-ray radiation in the radial direction. Top right: time-averaged radiation flux F_z^{re} due to the local photons from the local radiative processes and scattered photons originally from the central AGNs in the vertical direction. Middle left: time-averaged radiation flux $F_r^{c,\text{line}}$ due to the UV radiation from the AGNs in the radial direction. Middle right: time-averaged radiation flux F_z^{line} due to the UV radiation from the AGNs in the vertical direction. Bottom left: the distribution of the radiation fluxes with radius in the radial direction along $\theta = 71^\circ$. Bottom right: the distribution of the radiation fluxes with radius in the vertical direction along $\theta = 71^\circ$.

densities. Initially, low density gas for models 3, 5 and 7 is put in the computational domain with $\rho_0(r) = 2.25 \times 10^{-14} r_s^2 / r^2 \text{ g cm}^{-3}$, $\rho_0 = 10^{-25} \text{ g cm}^{-3}$ and $\rho_0 = 10^{-23} \text{ g cm}^{-3}$, respectively. In the region ($45^\circ < \theta < 60^\circ$), the injected winds have only few power.

The greater the initial density, the greater the optical depth, and the greater the wind resistance. Thus, the opening angle of winds narrows with the increase of initial density. In the winds region ($60^\circ < \theta < 80^\circ$), the winds go away at $\theta = 71^\circ$ and most of the

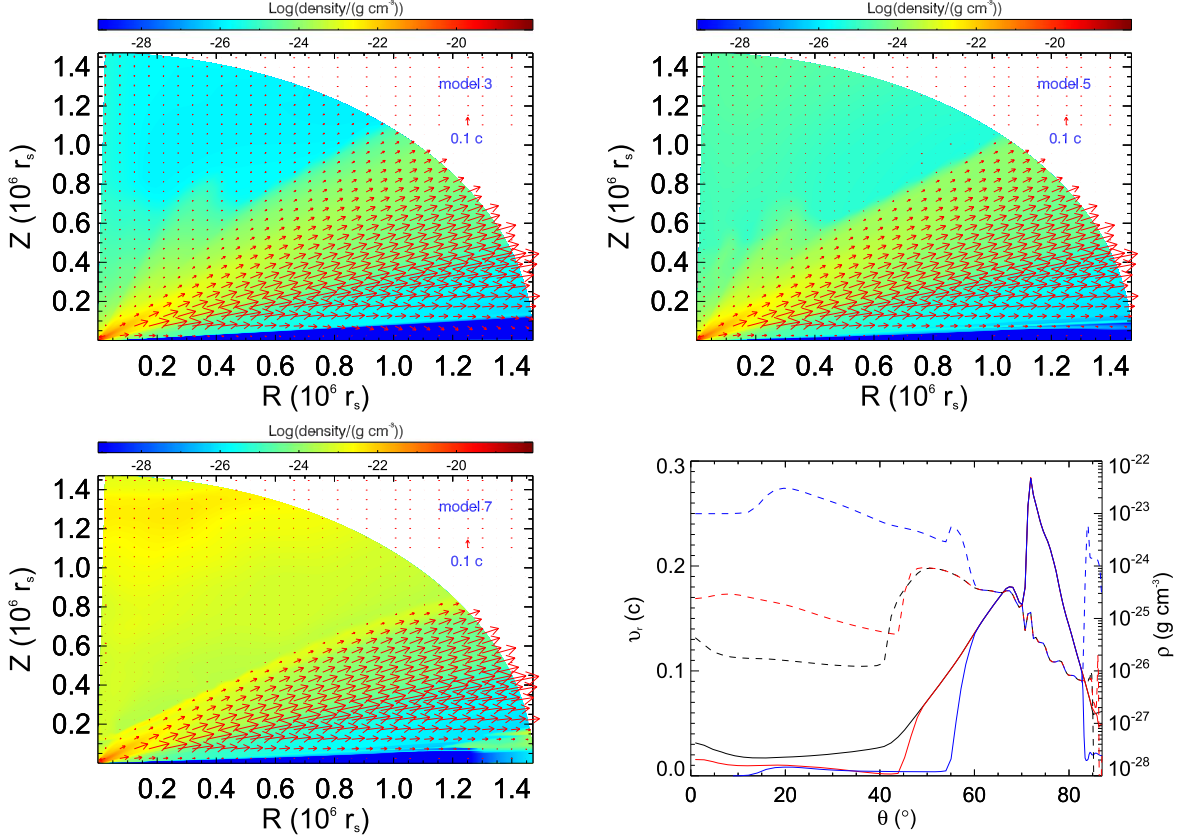


Figure 6. Comparison for models 3, 5 and 7. Top left: contours of gas density (color) and velocity (arrows) for model 3. Top right: contours of gas density (color) and velocity (arrows) for model 5. Bottom left: contours of gas density (color) and velocity (arrows) for model 7. Bottom right: angular distribution of the winds densities and velocities at outer boundary for models 3, 5 and 7 (black lines correspond to model 3, red lines correspond to model 5 and blue lines correspond to model 7), the ordinate on the left-hand side refers to the solid line, while the ordinate on the right-hand side refers to the dotted line. All the data in this figure are time-averaged.

kinetic energy flux is in this region. The injected winds have enough kinetic power to overcome the winds resistance. Therefore, the densities (velocities) of the winds, in the region ($60^\circ < \theta < 80^\circ$), are the same.

From Table 1, we can see that the significance of re-radiative effect depends on initial gas density. For the case of $M_{\text{BH}} = 10^8 M_\odot$, $\varepsilon = 0.6$, when $\rho_0 = 10^{-25} \text{ g cm}^{-3}$, the mass flux at the outer boundary for model 4 is approximately the same as model 5. But when $\rho_0 = 10^{-23} \text{ g cm}^{-3}$, the mass flux at the outer boundary increases by a factor of about 1.5 from model 6 to model 7. For $M_{\text{BH}} = 10^6 M_\odot$, $\varepsilon = 0.3$, when $\rho_0 = 10^{-25} \text{ g cm}^{-3}$, the mass flux at the outer boundary increases by a factor of about 2.6 from model 11 to model 12. But when $\rho_0 = 10^{-23} \text{ g cm}^{-3}$, the mass flux at the outer boundary increases by a factor of about 14 with the re-radiation effect. It is seen that the larger the gas density is, the stronger the re-radiation effect will be. Liu et al. (2013) also find that the larger density will produce the stronger re-radiation force. The reason is that the re-radiation force is proportional to the square

of the density while the gravitational force and gradient of gas pressure are proportional to the density (refer to Equation (14)).

3.4. Accretion Disk Luminosity Dependence

Zhu et al. (2022) find that in the case of $M_{\text{BH}} = 10^6 M_\odot$, $\varepsilon = 0.3$, the winds cannot escape from black hole potential. In this paper, we also study large-scale dynamics of the winds driven by the line force and the re-radiation force for $M_{\text{BH}} = 10^6 M_\odot$, $\varepsilon = 0.3$. The corresponding models are presented in Table 1. The mass flux of the injected winds (namely the mass flux measured at the inner boundary) is equal to $0.028370 L_{\text{edd}}/c^2$. From Table 1, it can be seen that the mass flux at the outer boundary increases by a factor of about 1.5 from model 9 to model 10, but these mass fluxes measured at the outer boundary are much smaller than that measured at the inner boundary. This indicates that the outflows do become much stronger with the re-radiation effect and the winds still cannot escape from gravitational potential.

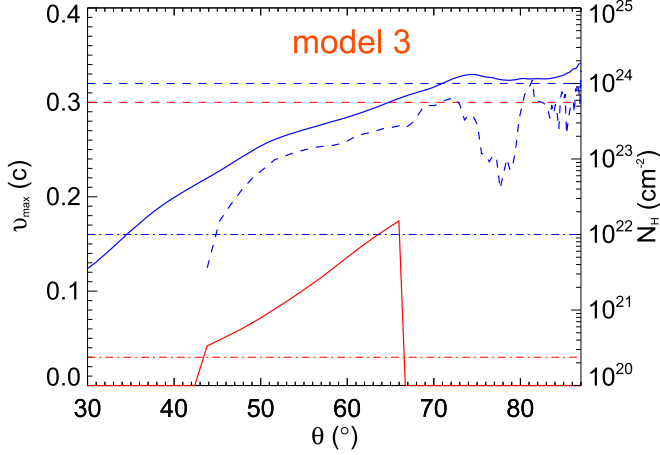


Figure 7. The θ dependence of time-averaged column density (solid blue line), column density of gas with $3 < \log \xi / (\text{erg cm s}^{-1}) < 6$ (dashed blue line), maximum velocity of winds with $3 < \log \xi / (\text{erg cm s}^{-1}) < 6$ (solid red line) at the outer boundary for the fiducial model. The red dotted-dashed line, the blue dotted-dashed line and the blue dashed line show the lines of $v_{\max} = 0.03c$, $v_{\max} = 0.3c$, $N_{\text{H}} = 10^{22} \text{ cm}^{-2}$ and $N_{\text{H}} = 10^{24} \text{ cm}^{-2}$, respectively. The ordinate on the left-hand side shows the velocity. The ordinate on the right-hand side shows the column density.

We can see from Table 1 that the significance of the re-radiative effect depends on accretion disk luminosity. For example, when $M_{\text{BH}} = 10^8 M_{\odot}$, $\varepsilon = 0.6$, the mass fluxes at the outer boundary are almost same for model 2 and model 3. But when $M_{\text{BH}} = 10^6 M_{\odot}$, $\varepsilon = 0.3$, the mass flux increases by a factor of about 1.5 from model 9 to model 10 (the initial density is same). The winds with the re-radiation force in the case of $M_{\text{BH}} = 10^6 M_{\odot}$, $\varepsilon = 0.3$ have a more obvious effect. This result is easy to understand. The mass flux in the case of $M_{\text{BH}} = 10^8 M_{\odot}$, $\varepsilon = 0.6$ is relatively large. Because of initially low density gas, the increase of the mass flux due to the re-radiation effect is negligibly small compared to the mass flux in the case of $M_{\text{BH}} = 10^8 M_{\odot}$, $\varepsilon = 0.6$. Thus, the mass flux for model 2 are almost same as that for model 3. For the case of $M_{\text{BH}} = 10^6 M_{\odot}$, $\varepsilon = 0.3$, the magnitude of the mass flux is comparable to the increase due to the re-radiation effect. Hence, it has a more visible result. The kinetic power of the winds is much lower than $0.5\% L_{\text{edd}}$, therefore, the winds might not affect the evolution of their host galaxies.

3.5. Comparison to Observations

Outflows from AGNs are one of the fundamental mechanisms for the interaction between the central supermassive black holes and their host galaxies. Observational evidences indicate that UFOs absorbers have been found in hard X-ray bands (6–9 keV) in ~ 40 percents of nearby AGNs (Pounds et al. 2003; Tombesi et al. 2010, 2011, 2012; Gofford et al. 2013, 2015; Laha et al. 2021). We define the UFOs with the outflows velocity spanning $v \sim 0.03\text{--}0.3c$, the ionization parameter $\xi \sim 10^3\text{--}10^6 \text{ erg cm s}^{-1}$

and the column density $10^{22} \text{ cm}^{-2} \leq N_{\text{H}} \leq 10^{24} \text{ cm}^{-2}$. It is found that the UFOs may be driven from accretion disk by line force (Nomura et al. 2016; Nomura & Ohsuga 2017; Yang et al. 2021; Zhu et al. 2022). In the large-scale simulations, we also find that UFOs are present. Figure 7 shows the view angle (θ) dependence of column density and velocity of the winds. The outflows over $44^{\circ}\text{--}66^{\circ}$ angle range satisfy the properties of UFOs in our fiducial model. The detection probability of UFOs is around 36%, which defines as $\Omega_{\text{UFO}}/4\pi$ (Nomura et al. 2016).

Gofford et al. (2015) perform a systematic analysis to the outflow properties in a sample of 51 Sukaku-observed AGNs and consider the properties of the associated winds. They find the mass flux of UFOs $\dot{M}_{\text{UFOs}} \propto L_{\text{D}}^{0.9}$ and the kinetic power of UFOs $\dot{E}_{\text{UFOs}} \propto L_{\text{D}}^{1.5}$. Nomura & Ohsuga (2017) and Zhu et al. (2022) perform two-dimensional simulations to study the dynamics of accretion disk winds driven by line force. It is found that the power law indexes are almost same as those given by the observations. Typically, the UFOs are detected that the mass outflows rate is $\sim 10^{24}\text{--}10^{26} \text{ g s}^{-1}$, and the kinetic luminosity of winds is constrained between $\sim 10^{43}\text{--}10^{45} \text{ erg s}^{-1}$. In our simulations, the winds found in this paper are driven by both the line force and re-radiation force. The mass outflow rate falls between 1.58×10^{25} and $1.35 \times 10^{26} \text{ g cm}^{-1}$, and the kinetic luminosity ranges between 2.72×10^{44} and $9.96 \times 10^{44} \text{ erg s}^{-1}$. The properties of the outflows are consistent with the observations. Therefore, the UFOs are quite probably driven by the combination of radiation line force and re-radiation force.

4. Discussions

In the paper, we gain time-averaged the simulation results at the outer boundary of the small scale simulations and inject the winds into the inner boundary of our large scale simulations. By using the time-averaged method, the properties of the high ionization winds can be erased due to their low density. Therefore, in the inner radial boundary of the large scale simulations, we mainly inject the low ionization winds. Thus, in the large scale simulations, we mostly explore the dynamics of the low ionization winds. It is too expensive to perfectly study the large scale dynamics of winds because of inner radial boundary located at close to the black hole and outer boundary located at beyond parsec scale.

In our simulations, we set $\sigma_{\text{X}} = 100\sigma_{\text{e}}$ for $\xi < 10^5 \text{ erg cm s}^{-1}$ and $\sigma_{\text{X}} = \sigma_{\text{e}}$ for $\xi \geq 10^5 \text{ erg cm s}^{-1}$ (Proga et al. 2000; Nomura & Ohsuga 2017; Yang et al. 2021; Zhu et al. 2022), which is inherent limitation in the current setup of hydrodynamics for line-driven disk winds simulations. The abrupt switch due to the step function is arbitrary. For example, the X-rays are heavily attenuated below $\xi = 10^5 \text{ erg cm s}^{-1}$ from $\sigma_{\text{X}} = \sigma_{\text{e}}$ to $\sigma_{\text{X}} = 100\sigma_{\text{e}}$, resulting in very effective shielding. In the case UV radiation, $\sigma_{\text{UV}} = \sigma_{\text{e}}$ for the entire range of ξ . This processing method is physically inconsistent with the absorption of ultraviolet radiation by wind material through bound transitions. Proga & Kallman (2004) also explore the situation

of $\sigma_X = \sigma_e$ for all ξ . Nomura et al. (2020) compare the results of these two methods and find that the mass fluxes of winds differ roughly by a factor of 2. However, we note that both of the treatments are arbitrary. In future work, we plan to study more realistic physical models of X-ray and UV opacities.

Sim et al. (2010) and Higginbottom et al. (2014) indicate that scattered X-ray photons also contribute to gas ionization with the postprocessed radiation transfer calculations. However, radiative transfer and hydrodynamics are decoupled in those papers. The simulation of actual flows requires coupling radiation transfer and HD/MHD calculations, which are not realistic due to the large computational costs. In this paper, we perform the hydrodynamics simulations of line-driven winds with the re-radiation effect. We include the radiation force caused by the scattered and reprocessed photons in the momentum equation. Although the scattered and reprocessed photons are included in the paper, our treatments for calculating the winds photoionization structure and the interaction between the radiation are oversimplified. The next generation code of HD/MHD formalism is urgent on principle, which can handle radiative transfer in a more realistic and detailed manner.

In addition, the magnetic field is always present. The inclusion of magnetic field will enhance the outflows and produce winds with a broader opening angle (Kuncic & Bicknell 2007; Cui & Yuan 2020b; Yang et al. 2021;). The standard magnetorotational instability (SMRI) has been directly observed in a Taylor-Couette cell with independently rotating and electrically conducting end caps and is responsible for causing the angular momentum transfer (Balbus & Hawley 1991; Wang et al. 2022a, 2022b). It is interesting to study the large-scale dynamics of winds driven by combining the radiation and magnetic field in future.

5. Summary

We carry out two-dimensional simulations to study the large-scale dynamics of accretion disk winds driven by radiation line force and re-radiation force. We study the properties of the winds with the re-radiation effect around parsec scale. It is currently impossible to perform simulations with the inner boundary close to the black hole and outer boundary around parsec scale. Therefore, we divide the space scale into small scale and large scale. For the small scale simulations, the computational domain is $30r_s \leq r \leq 1500r_s$. The winds are driven by radiation line force. For our large scale simulations, the computational domain covers $1500r_s \leq r \leq 1.5 \times 10^6 r_s$. The locally generated photons through scattering, bremsstrahlung and line radiation in the gas can also play an important role. The dynamics of the winds at large scale is driven by the combination of radiation line force and re-radiation force. We inject winds at the inner radial boundary ($1500r_s$) which are time-average obtained by the small scale simulations.

Including the gravitational potential of host galaxy has little impact on the large-scale dynamics of the winds. For

$M_{\text{BH}} = 10^8 M_\odot$, $\varepsilon = 0.6$, the properties of the winds are the same. In the case of $M_{\text{BH}} = 10^6 M_\odot$, $\varepsilon = 0.3$, the mass flux at the outer boundary slightly decreases and momentum flux and kinetic energy flux reduce to about 90% with the galaxy potential. However, those fluxes measured at the outer boundary are too little and the winds cannot escape from gravitational potential.

Taking the fiducial model as an example, we find that the re-radiation force drives stronger outflows at the first period of time. As Mosallanezhad et al. (2019) found, the outflow rate of the accretion flows at the outer boundary is enhanced. When the flows get into the steadiness, however, the radiation flux due to photoionization heating-recombination cooling, X-ray radiation, and the local photons from the local radiative processes and scattered photons can almost be neglected and the UV radiation due to spectral lines dominates total radiation. Thus, the properties of the winds are almost the same when the quasi-steady state has been formed. The kinetic power of the winds is significantly higher than $0.5\%L_{\text{edd}}$, so the winds can provide sufficient feedback to their host galaxies (Di Matteo et al. 2005; Hopkins & Elvis 2010; Bu & Yang 2021).

We find that initial gas density can affect the properties of the winds driven by radiation line force and re-radiation force. In our models, low density gas is put in the computational domain with $\rho_0(r) = 2.25 \times 10^{-14} r_s^2 / r^2 \text{ g cm}^{-3}$, $\rho_0 = 10^{-25} \text{ g cm}^{-3}$, and $\rho_0 = 10^{-23} \text{ g cm}^{-3}$. The opening angle of winds narrows with the increase of initial density. Moreover, the significance of re-radiative effect depends on initial gas density. The larger the gas density is, the stronger the re-radiation effect will be. We also study the accretion disk luminosity dependence. For the case of $M_{\text{BH}} = 10^6 M_\odot$, $\varepsilon = 0.3$, the magnitude of the mass flux is comparable to the increase due to the re-radiation effect. Thus, it has a more visible result. The kinetic power of the winds is much lower than $0.5\%L_{\text{edd}}$, therefore, the winds might not affect the evolution of their host galaxies.

We compare our simulations results to observations. The observed dependence of kinetic power and mass flux on the accretion disk luminosity can be well produced Gofford et al. (2015), Nomura & Ohsuga (2017), Zhu et al. (2022). For the UFOs found in hard X-ray bands, the detection probability of UFOs and the properties of the winds in our fiducial model are both consistent with observations. Therefore, the UFOs are quite probably driven by the combination of radiation line force and re-radiation force.

ORCID iDs

Yi Zhu  <https://orcid.org/0000-0002-9638-6803>

References

- Ajello, M., et al. 2021, *ApJ*, **921**, 144
 Almeida, L., Nemmen, R., Wong, K. W., et al. 2018, *MNRAS*, **475**, 5398
 Balbus, S. A., & Hawley, J. F. 1991, *ApJ*, **376**, 214

- Begelman, M. C., McKee, C. F., & Shields, G. A. 1983, *ApJ*, 271, 70
- Blandford, R., & Payne, D. G. 1982, *MNRAS*, 199, 883
- Blondin, J. M. 1994, *ApJ*, 435, 756
- Bu, D. F., & Gan, Z. M. 2018, *MNRAS*, 474, 1206
- Bu, D. F., & Yang, X. H. 2021, *ApJ*, 921, 100
- Bu, D. F., Yuan, F., Gan, Z. M., & Yang, X. H. 2016, *ApJ*, 818, 83
- Cao, X. W. 2014, *ApJ*, 783, 51
- Ciotti, L., Ostriker, J. P., & Proga, D. 2009, *ApJ*, 699, 89
- Crenshaw, D. M., Kraemer, S. B., & George, I. M. 2003, *ARA&A*, 41, 117
- Cui, C., & Yuan, F. 2020b, *ApJ*, 890, 81
- Cui, C., Yuan, F., & Li, B. 2020, *ApJ*, 890, 80
- Di Matteo, T., Springel, V., & Hernquist, L. 2005, *Nature*, 433, 604
- Díaz Trigo, M., & Boirin, L. 2016, *AN*, 337, 368
- Dye, S., Evans, N. W., Belokurov, V., et al. 2008, *MNRAS*, 388, 384
- Gofford, J., Reeves, J. N., McLaughlin, D. E., et al. 2015, *MNRAS*, 451, 4169
- Gofford, J., Reeves, J. N., Tombesi, F., et al. 2013, *MNRAS*, 430, 60
- He, Z. C., Wang, T. G., Liu, G. L., et al. 2019, *NatAs*, 3, 265
- Higginbottom, N., Proga, D., Knigge, C., Long, K. S., et al. 2014, *ApJ*, 789, 19
- Higginbottom, N., Proga, D., Knigge, C., & Long, K. S. 2017, *ApJ*, 836, 42
- Homan, J., Neilsen, J., Allen, J. L., et al. 2016, *ApJL*, 830, L5
- Hopkins, P. F., & Elvis, M. 2010, *MNRAS*, 401, 7
- King, A., & Pounds, K. 2015, *ARA&A*, 53, 115
- Kuncic, Z., & Bicknell, G. V. 2007, *MPLA*, 22, 1685
- Laha, S., Reynolds, C. S., Reeves, J., et al. 2021, *NatAs*, 5, 13
- Lin, X. Z., Xue, Y. Q., Fang, G. W., et al. 2022, *RAA*, 22, 015010
- Liu, C., Gan, F. M., & Xie, F. G. 2013, *RAA*, 13, 899
- Liu, C., Yuan, F., Ostriker, J. P., et al. 2013, *MNRAS*, 434, 1721
- Ma, R., Roberts, S. R., Li, Y., et al. 2019, *MNRAS*, 483, 5614
- Mignone, A., Bodo, G., Massaglia, S., et al. 2007, *ApJS*, 170, 228
- Mignone, A., Zanni, C., Tzeferacos, P., et al. 2012, *ApJS*, 198, 7
- Mosallanezhad, A., Yuan, F., Ostriker, J. P., Zeraatgari, F. Z., & Bu, D.-F. 2019, *MNRAS*, 490, 2567
- Munoz-Darias, T., Jimenez-Ibarra, F., et al. 2019, *ApJ*, 879, 4
- Narayan, R., Sadowski, A., Penna, R. F., & Kulkarni, A. K. 2012, *MNRAS*, 426, 3241
- Neilsen, J., & Homan, J. 2012, *ApJ*, 750, 27
- Nomura, M., & Ohsuga, K. 2017, *MNRAS*, 465, 2873
- Nomura, M., Ohsuga, K., & Done, C. 2020, *MNRAS*, 494, 3616
- Nomura, M., Ohsuga, K., Takahashi, H. R., et al. 2016, *PASJ*, 68, 16
- Ostriker, J. P., Choi, E., Ciotti, L., et al. 2010, *ApJ*, 722, 642
- Paczynsky, B., & Wiita, P. J. 1980, *A&A*, 88, 23
- Pounds, K. A., Reeves, J. N., King, A. R., et al. 2003, *MNRAS*, 345, 705
- Proga, D., & Kallman, T. R. 2004, *ApJ*, 616, 688
- Proga, D., Stone, J. M., & Drew, J. E. 1998, *MNRAS*, 295, 595
- Proga, D., Stone, J. M., & Kallman, T. R. 2000, *ApJ*, 543, 686
- Shakura, N. I., & Sunyaev, R. A. 1973, *A&A*, 24, 337
- Shi, F. Z., Li, Z. Y., Yuan, F., et al. 2021, *NatAs*, 5, 928
- Sim, S. A., Proga, D., Miller, L., et al. 2010, *MNRAS*, 408, 1396
- Stevens, I. R., & Kallman, T. R. 1990, *ApJ*, 365, 321
- Tombesi, F., Cappi, M., Reeves, J. N., et al. 2010, *A&A*, 521, 57
- Tombesi, F., Cappi, M., & Reeves, J. N. 2012, *MNRAS*, 422, L1
- Tombesi, F., Tazaki, F., Mushotzky, R. F., et al. 2014, *MNRAS*, 443, 2154
- Tombesi, T., Cappi, M., Reeves, J. N., et al. 2011, *ApJ*, 742, 44
- Wang, Y., Gilson, E. P., Ebrahimi, F., et al. 2022a, *NatCo*, 13, 4679
- Wang, Y., Gilson, E. P., Ebrahimi, F., et al. 2022b, *PhRvL*, 129, 115001
- Weinberger, R., Springel, V., Hernquist, L., et al. 2017, *MNRAS*, 465, 3291
- Woods, D. T., Klein, R. I., Castor, J. I., et al. 1996, *ApJ*, 461, 767
- Yang, X. H. 2021b, *ApJ*, 922, 262
- Yang, X. H., Ablimit, K., & Li, Q. X. 2021, *ApJ*, 914, 31
- You, B., Straub, O., Czerny, B., et al. 2016, *ApJ*, 821, 104
- Yuan, F., Bu, D. F., & Wu, M. C. 2012, *ApJ*, 761, 130
- Yuan, F., Gan, Z., Narayan, R., et al. 2015, *ApJ*, 804, 101
- Yuan, F., & Narayan, R. 2014, *ARA&A*, 52, 529
- Yuan, F., Yoon, D., Li, Y., et al. 2018, *ApJ*, 857, 121
- Zhang, T. C., Guo, Q., Qu, Y., et al. 2021, *RAA*, 21, 212
- Zhu, Y., Bu, D. F., Yang, X. H., Yuan, F., & Lin, W. B. 2022, *MNRAS*, 513, 1141